Astronomy & Astrophysics manuscript no. output
August 26, 2021

Pulsating hydrogen-deficient white dwarfs and pre-white dwarfs observed with *TESS*

III. Asteroseismology of the DBV star GD 358

Alejandro H. Córsico[1,2], Murat Uzundag[3,4], S. O. Kepler[5], Roberto Silvotti[6], Leandro G. Althaus[1,2], Detlev Koester[7], Andrzej S. Baran[8,9,10], Keaton J. Bell[11,12], Agnès Bischoff-Kim[13], J. J. Hermes[14], Steve D. Kawaler[15], Judith L. Provencal[16,17], Don E. Winget[18,19], Michael H. Montgomery[18,19], Paul A. Bradley[20], S. J. Kleinman[21], and Atsuko Nitta[21]

[1] Grupo de Evolución Estelar y Pulsaciones. Facultad de Ciencias Astronómicas y Geofísicas, Universidad Nacional de La Plata, Paseo del Bosque s/n, 1900 La Plata, Argentina
[2] IALP - CONICET
[3] Instituto de Física y Astronomía, Universidad de Valparaiso, Gran Bretaña 1111, Playa Ancha, Valparaíso 2360102, Chile
[4] European Southern Observatory, Alonso de Cordova 3107, Santiago, Chile
[5] Instituto de Física, Universidade Federal do Rio Grande do Sul, 91501-900, Porto-Alegre, RS, Brazil
[6] INAF-Osservatorio Astrofisico di Torino, strada dell'Osservatorio 20, 10025 Pino Torinese, Italy
[7] Institut für Theoretische Physik und Astrophysik, Universität Kiel, 24098 Kiel, Germany
[8] ARDASTELLA Research Group, Institute of Physics, Pedagogical University of Krakow, ul. Podchorążych 2, 30-084 Kraków, Poland
[9] Embry-Riddle Aeronautical University, Department of Physical Science, Daytona Beach, FL 32114, USA
[10] Department of Physics, Astronomy, and Materials Science, Missouri State University, Springfield, MO 65897, USA
[11] DIRAC Institute, Department of Astronomy, University of Washington, Seattle, WA-98195, USA
[12] NSF Astronomy and Astrophysics Postdoctoral Fellow
[13] Penn State Worthington Scranton, Dunmore, PA 18512, USA
[14] Department of Astronomy, Boston University, Boston, MA-02215, USA
[15] Department of Physics and Astronomy, Iowa State University, Ames, IA 50011, USA
[16] University of Delaware, Department of Physics and Astronomy Newark, DE 19716, USA
[17] Delaware Asteroseismic Research Center, Mt. Cuba Observatory, Greenville, DE 19807, USA
[18] Department of Astronomy, University of Texas at Austin, Austin, TX-78712, USA
[19] McDonald Observatory, Fort Davis, TX-79734, USA
[20] XCP-6, MS F-699 Los Alamos National Laboratory, Los Alamos, NM 87545, USA
[21] Gemini Observatory/NSF's NOIRLab, 670 N. A'ohoku Place, Hilo, Hawai'i, 96720, USA

Received ; accepted

ABSTRACT

Context. The collection of high-quality photometric data through space missions, such as the already completed *Kepler* mission and the ongoing *TESS* program, is revolutionizing the area of white-dwarf asteroseismology. Among the different kinds of pulsating white dwarfs, there are those that have He-rich atmospheres, and they are called DBVs or V777 Her variable stars. The archetype of these pulsating white dwarfs, GD 358, is the focus of the present paper.

Aims. We present a detailed asteroseismological analysis of the DBV star GD 358 based on the observations collected by the *TESS* mission combined with ground-based data.

Methods. We processed and analyzed *TESS* observations of the already known DBV star GD 358 (TIC 219074038). We performed a detailed asteroseismological analysis of this star using DB white-dwarf evolutionary models that take into account the complete evolution of the progenitor stars. We constrained the mass of this star by comparing the observed period spacing with the period spacings of the models, and we employed the individual observed periods to search for a representative seismological model. We detected potential frequency multiplets for GD 358, which we use to identify the harmonic degree (ℓ) of the pulsation modes and rotation period.

Results. In total, we extracted 26 periodicities from the *TESS* light curve of this DBV star using a standard pre-whitening. The oscillation frequencies are associated with g-mode pulsations with periods spanning $\sim$ 422 s to $\sim$ 1087 s. Moreover, we detected 8 combination frequencies between $\sim$ 543 s to $\sim$ 295 s. We combine these data with a huge amount of observations from the ground. We find a constant period spacing of 39.25 $\pm$ 0.17 s, which allowed us to infer its mass ($M_\star = 0.581 \pm 0.031 M_\odot$) and constrain the harmonic degree ℓ of the modes. We performed a period-to-period fit analysis on GD 358, and we were able to find an asteroseismological model with a stellar mass ($M_\star = 0.584^{+0.025}_{-0.019} M_\odot$) in agreement with the inferred from the period spacing, and compatible with the spectroscopic mass ($M_\star = 0.560 \pm 0.028 M_\odot$). In agreement with previous works, we found that the frequency splittings vary according to the radial order of the modes, suggesting differential rotation. Obtaining a seismological model allowed us to estimate the seismological distance ($d_{\rm seis} = 42.85 \pm 0.73$ pc) of GD 358, which is in excellent agreement with the precise astrometric distance measured by *GAIA* EDR3 ($\pi = 23.244 \pm 0.024, d_{\rm GAIA} = 43.02 \pm 0.04$ pc).

Conclusions. The high-quality data collected by the *TESS* space mission, considered simultaneously with ground-based observations, are able to provide valuable input to the asteroseismology of DBV stars, similar to the case of other classes of pulsating white-dwarf stars. The *TESS* mission, in conjunction with future space missions and upcoming surveys, will allow for substantial progress in white-dwarf asteroseismology.

Key words. stars — pulsations — stars: interiors — stars: evolution — stars: white dwarfs

1. Introduction

Pulsating white dwarfs (WD) and pre-WDs constitute a long-studied and reliably established class of compact variable stars, both from an observational point of view and from theoretical grounds. Their brightness variations are multiperiodic, with periods between 100 s and 7 000 s, and amplitudes up to 0.4 mag in typical optical light curves (see the reviews by Winget & Kepler 2008; Fontaine & Brassard 2008; Althaus et al. 2010; Córsico et al. 2019). The variability is associated to low-degree ($\ell \leq 2$) nonradial g(gravity)-mode pulsations excited by a physical mechanism related to the partial ionization of the dominant chemical species in the zone of driving, located in the outer layers. In the case of warm and cool pulsating WDs, the opacity bumps associated to these partial-ionization zones are responsible for the appearance of an outer convection zone, which also strongly contributes to g-mode pulsation instabilities (Brickhill 1991; Goldreich & Wu 1999; Wu & Goldreich 1999). The first pulsating WD was discovered in 1968 (Landolt 1968), and currently more than 300 objects are known. They are classified in various categories, including ZZ Ceti stars or DAVs (pulsating hydrogen-rich WDs), V777 Her stars or DBVs (pulsating helium-rich WDs), and GW Vir stars or pulsating PG1159 stars, among others (Winget & Kepler 2008; Fontaine & Brassard 2008; Althaus et al. 2010; Córsico et al. 2019).

Since the discovery of the first pulsating WDs, observations of these variable stars have been steadily increasing, thanks to single-site observations and also multi-site campaigns like those of the Whole Earth Telescope (*WET*; Nather et al. 1990). Subsequently, a dramatic growth in the number of known pulsators was made possible thanks to the identification of candidates from the spectral observations of the Sloan Digital Sky Survey (SDSS, York et al. 2000; Kleinman et al. 2013; Kepler et al. 2015, 2016, 2019a). Finally, in recent years, the area has received a strong boost driven by the uninterrupted observations from space made by the *Kepler* telescope, both main mission (Borucki et al. 2010) and *K2* mode (Howell et al. 2014). Indeed, these efforts allowed the study of 32 ZZ Ceti stars and two DBV stars (Østensen et al. 2011; Hermes et al. 2017a,b; Bell et al. 2017; Bell 2017; Córsico 2020), until the spacecraft ran out of fuel in 2018. The successor to *Kepler* is the Transiting Exoplanet Survey Satellite (*TESS*, Ricker et al. 2015). This space mission has observed 200 000 brightest stars in 85% of the whole sky in 2019 and 2020 in the first part of the mission. *TESS* performs extensive time-series photometry that allows to discover pulsating stars, and, in particular, variable hot subdwarfs, WDs, and pre-WDs with mag < 16, with short (120 s) cadence. Starting in July 2020, it is now also observing in 20 s cadence.

Relevant to this work are the DBV stars, which are pulsating He atmosphere WDs with effective temperatures in the range $22\,400 \lesssim T_{\rm eff} \lesssim 32\,000$ K and pulsate with g-mode periods between 120 and 1080 s (Winget & Kepler 2008; Córsico et al. 2019). The existence of the DBV class of pulsating WDs was anticipated through theoretical arguments (Winget et al. 1982b) before it was confirmed observationally shortly after (Winget et al. 1982a). Pulsations in DBVs are thought to be excited by a combination of the κ mechanism acting in the He partial ionization zone — and thus setting the blue edge of the DBV instability strip (Winget et al. 1983b), and the "convective driving" mechanism (Brickhill 1991) which is possibly dominant once the outer convection zone has deepened enough (see the time-dependent convection analyses of Dupret et al. 2008; Quirion et al. 2008; Van Grootel et al. 2017).

As a result of the high-quality *Kepler* and *K2* observations, two DBV stars, KIC 8626021 (Østensen et al. 2011) and PG 0112+104 (Hermes et al. 2017b), were intensively studied with space data. In particular, KIC 8626021 has been the focus of intense modeling by several independent research groups (Bischoff-Kim & Østensen 2011; Córsico et al. 2012; Bischoff-Kim et al. 2014; Giammichele et al. 2018; Charpinet et al. 2019), who have explored its internal structure with unprecedented precision. The first DBV pulsator observed extensively with *TESS* is EC 0158−160 or WD 0158−160 (TIC 257459955), which was studied and modelled in detail by Bell et al. (2019). This star was an already known DBV pulsator with $T_{\rm eff} = 24\,130 \pm 1369$ K and $\log g = 7.94 \pm 0.03$ (Rolland et al. 2018), or alternatively, $T_{\rm eff} = 25\,518 \pm 1000$ K and $\log g = 7.875 \pm 0.06$ (Voss et al. 2007). Bell et al. (2019) find nine independent frequencies suitable for asteroseismology. A mean period spacing $\Delta\Pi = 38.1 \pm 1.0$ s for $\ell = 1$ modes, is present in the period data. A comparison with the average of the models period spacing indicates a stellar mass of $M_\star = 0.621 \pm 0.06 M_\odot$, or alternatively, $M_\star = 0.658 \pm 0.10 M_\odot$ (according to the two different spectroscopic determinations of $T_{\rm eff}$), larger than the spectroscopic estimates ($M_\star = 0.542 - 0.557 M_\odot$). The star also has been analysed by performing period-to-period fits by employing a fully evolutionary model approach (see, e.g., Córsico et al. 2012) and a parametric evolutionary model approach (see, e.g., Bischoff-Kim & Montgomery 2018). The asteroseismological solution that satisfies both the spectroscopic parameters and the astrometric constraints from *Gaia* is characterized by a DB white dwarf model with $M_\star \sim 0.60\ M_\odot$, $T_{\rm eff} \sim 25\,600$ K, $\log(M_{\rm He}/M_\star) \sim -1.52$, $d \sim 67$ pc, and a rotation period of ~ 7 or ~ 14 hours.

In this work, we present new *TESS* observations of the already known DBV star GD 358. We perform a detailed asteroseismological analysis of this star on the basis of the fully evolutionary models of DB WDs computed by Althaus et al. (2009). The present study is the third part of our series of papers devoted to the study of pulsating H-deficient WDs observed with *TESS*. The first article is focused on six already known GW Vir stars (Córsico et al. 2021), and the second one is devoted to the discovery of two new GW Vir stars, specifically DOVs (Uzundag et al. 2021).

The paper is organized as follows. In Section 2 we provide a brief account of the main characteristics of GD 358. In Sect. 3, we describe the methods we apply to obtain the pulsation periods of the target star. A brief summary of the stellar models of DB WD stars employed for the asteroseismological analysis of GD 358 is provided in Sect. 4. Sect. 5 is devoted to the asteroseismological modelling of the target star, including the search for a constant period spacing in the set of periods by applying three significance tests, the assessing of the stellar mass through the use of the period spacing, and by performing a period-to-period fit with the aim of finding an asteroseismological model. Finally, in Sect. 6, we summarize our main results and make some concluding remarks.

2. The target star: GD 358

The location of GD 358 in the $\log T_{\rm eff}$ versus $\log g$ diagram is displayed in Fig. 1. We describe the basic characteristics of this star below and summarize its stellar properties in Table 1.

GD 358 (or V777 Her) has a *TESS* Input Catalog (TIC) number TIC 219074038. It is the brightest ($m_{\rm V} = 13.7$) and most extensively studied DBV star. This prototypical object provides the designation for the class of V777 Her (or DBV) variable stars.

Table 1. Characteristics of GD 358. Columns 1, 2, 3, 4, 5, and 6 correspond to the *TESS* input catalog number, name of the object, effective temperature, surface gravity, Gaia EDR3 parallax, and distance, respectively.

TIC	Name	$T_{\rm eff}$ [K]	$\log g$ [cgs]	π [mas]	d [pc]
219074038	GD 358 (V777 Her)	24 937 ± 1018	7.92 ± 0.05	23.244 ± 0.024	43.02 ± 0.04
		24 000 ± 500	7.80 ± 0.05		

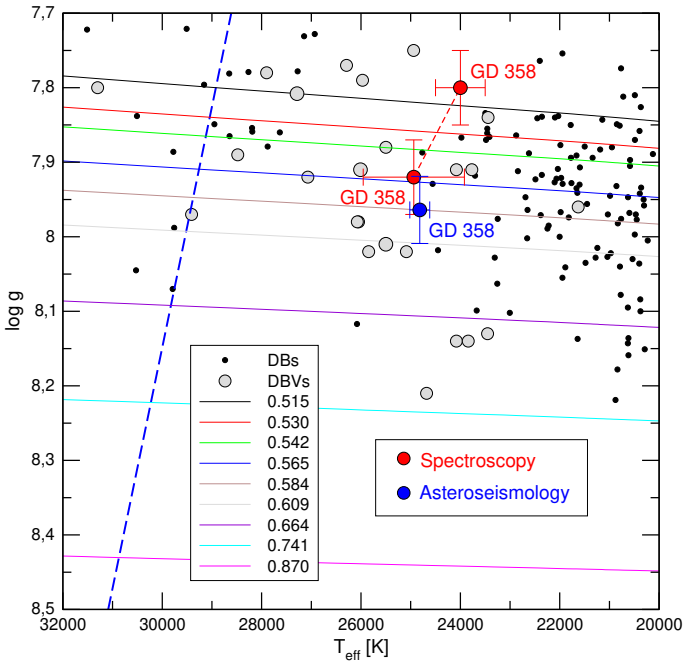

Fig. 1. Location of DB WDs on the $T_{\rm eff} - \log g$ diagram (Kepler et al. 2019b), marked with small black circles. Also depicted is the location of the published DBV stars (gray circles), according to the compilation by Córsico et al. (2019). The target star of the present paper, GD 358, is highlighted with large red circles according to spectroscopy, being the two locations of corresponding to the two spectroscopic determinations of $T_{\rm eff}$ and $\log g$ according to Koester et al. (2014) and Bédard et al. (2017). The location of the asteroseismological model (see Sect. 5.2) is emphasized with a blue circle. The DB WD evolutionary tracks of Althaus et al. (2009) are displayed with different colours according to the stellar-mass values (in solar units). The blue-dashed line represents the theoretical dipole ($\ell = 1$) blue edge of the DBV instability strip, according to Córsico et al. (2009).

GD 358 was discovered to pulsate in 1982 (Winget et al. 1982b). Its spectroscopic surface parameters are $T_{\rm eff} = 24\,937 \pm 1018$ K and $\log g = 7.92 \pm 0.05$ according to Bédard et al. (2017) from optical data (see Fig.1), although the previous analysis by Nitta et al. (2012) and Koester et al. (2014) using optical and UV data give $T_{\rm eff} = 24\,000 \pm 500$ K and $\log g = 7.8 \pm 0.05$ (Fig.1). GD 358 has been extensively observed by the *WET* collaboration (Winget et al. 1994; Vuille et al. 2000; Kepler et al. 2003; Provencal et al. 2009). The most recent and complete analysis of this star has been carried out by Bischoff-Kim et al. (2019), who collected and reduced data from 34 years of photometric observations, including archival data from 1982 to 2006, and 1195.2 hr of observations from 2007 to 2016. Bischoff-Kim et al. (2019) detected a total of 15 independent periods, of which thirteen belong to a series of $\ell = 1$ pulsation periods with consecutive radial order, the longest continuous sequence of periods observed in a DBV star until then. The star has repeatedly been the focus of asteroseismological analyses (Bradley & Winget 1994; Metcalfe et al. 2000, 2001; Fontaine & Brassard 2002; Metcalfe 2003) using evolutionary models of DB WDs with simplified chemical profiles. Bischoff-Kim et al. (2019) analysed this star using models that include parameterized, complex, core-composition profiles to fit the 15 observed periods. They obtain a seismological model with a thickness of the He layer that is qualitatively consistent with the diffusion-calculation picture that predict that the pure-He envelope will steadily grow thicker as the DB star cools (Dehner & Kawaler 1995; Fontaine & Brassard 2002; Althaus & Córsico 2004). The *Gaia* EDR3 parallax and distance for GD 358 are $\pi = 23.244 \pm 0.024$ mas and $d = 43.02 \pm 0.04$ pc (Bailer-Jones et al. 2021), respectively.

3. Observations and data reduction

GD 358 was observed by *TESS* at 2-min cadence on Sector 25 between 2020-May-13 and 2020-June-08, targeted as TIC 219074038 (T=13.9 mag). The temporal resolution is $1/T = 0.451$ μHz (T is the data span of 25.67 days). The light curve for GD 358 released by the Science Processing Operations Center (SPOC) pipeline had large gaps, which we believe were caused by unnecessarily harsh clipping based on quality flags that resulted in a low (67.4%) duty cycle. We re-reduced the Sector 25 data with the same 5-pixel aperture from the SPOC pipeline but with a looser quality-flag cuts, yielding a significantly higher (92.6%) duty cycle. Our final light curve was flattened of long-term trends by the division of second-order polynomial every 2 days. The final light curve is shown in Fig. 2 including 16781 data points spanning 25 days.

The average noise level of the amplitude spectra is 0.24 ppt. We calculated a detection threshold of 0.1% false alarm probability (FAP) following the method described in Kepler (1993). If the amplitude of a given peak above this value, there is a 0.1% chance that of resulting from random noise fluctuations. All frequencies are above the threshold level of 0.1% FAP of 1.45 ppt have been prewhitened a few exceptions. The frequencies at 1657 and 2157 μHz are below the significance threshold with S/N of 5.6 and 4.6 respectively. These frequencies were reported in previous work by Bischoff-Kim et al. (2019). Moreover, we prewhitened 8 combination frequencies, which are located at beyond 2300 μHz. A few of them at 2315, 2530, 2912 and 3386 μHz are slightly below 0.1% FAP level with S/N of 5.3, 5.5, 4.7 and 5 respectively. All combination frequencies beyond 2400 μHz are detected for the first time and also extracted from the light curve and reported in Table 3. Overall, we have detected 26 frequencies that are concentrated between 900 μHz and 3400 μHz, out of which we identified 8 combination frequencies. Fig. 2 displays the Fourier transform of GD 358. In Table 3 we show the list of periods of GD 358 detected with *TESS*.

The frequencies emphasized with boldface in Table 3 are components of rotational triplets ($\ell = 1$). Rotational multiplets are depicted in Fig. 3. Here, we briefly describe the effect of rotation on the pulsation frequencies of a star. In the presence of

Table 2. Parameters of the *TESS* observations of GD 358, including observed sectors, *TESS* magnitude along with name of the targets, the date and length of the runs (columns 1, 2, 3, 4, 5 and 6). After Fourier transform, three different set of parameters (resolution, average noise level of amplitude spectra and the detection threshold which is defined as 0.1% false alarm probability (FAP)) are presented in columns 7, 8 and 9, respectively.

TIC	Name	$T_{\rm mag}$	Obs. Sector	Start Time (BJD-2 457 000)	Length [d]	Resolution μHz	Average Noise Level [ppt]	0.1% FAP [ppt]
219074038	GD 358 (V777 Her)	13.59	25	1983.6362	25.00	0.46	0.24	1.45

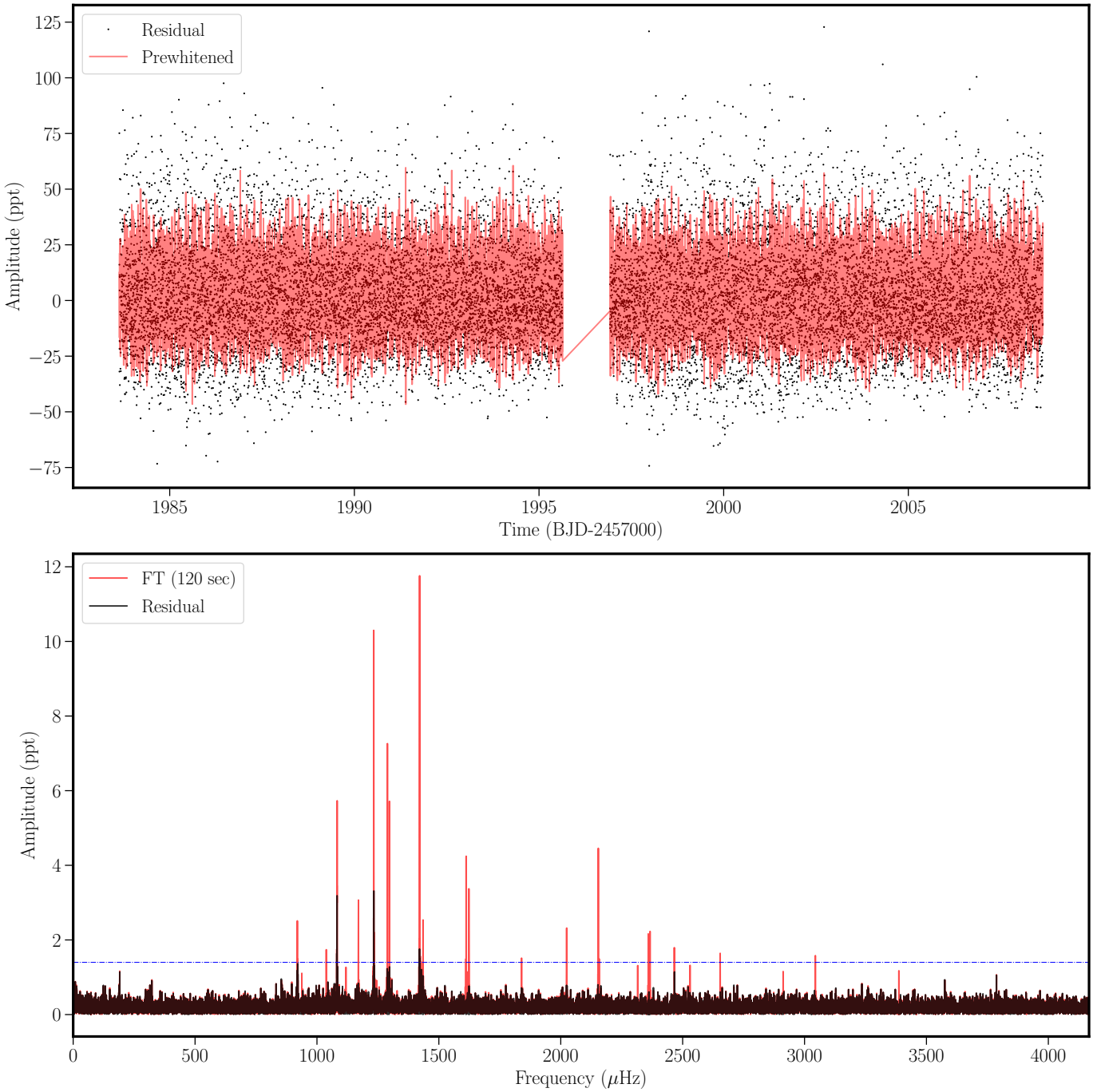

Fig. 2. TOP: The light curve of the pulsating DBV star GD 358 observed in sector 25. The black dots show the residual flux while the red lines show all prewhitened variations from the light curve. BOTTOM: Fourier transform of the pulsating DBV star GD 358 observed with 120-sec cadence. The dotted horizontal blue line indicates the 0.1% false-alarm-probability (FAP) significance threshold. The black line is the FT of the prewhitened light curve.

stellar rotation, non-radial modes of degree ℓ split into $2\ell + 1$ components differing in azimuthal (m) number. In the case of slow and solid rotation, the frequency splitting can be obtained as: $\delta\nu_{\ell,k,m} = m\ (1 - C_{\ell,k})\ \Omega_{\rm R}$, $\Omega_{\rm R}$ being the rotational angular frequency of the pulsating star, and $m = 0, \pm1, \pm2, \cdots, \pm\ell$. The condition of slow rotation translates in $\Omega_{\rm R} \ll \nu_{\ell,k}$. The coefficients $C_{\ell,k}$, called Ledoux coefficients (Ledoux & Walraven 1958), adopt a simple form in the asymptotic limit of high radial-order g modes ($k \gg \ell$): $C_{\ell,k} \sim [\ell(\ell+1)]^{-1}$. For dipole ($\ell = 1$) and quadrupole ($\ell = 2$) modes, we have $C_{1,k} \sim 0.5$ and $C_{2,k} \sim 0.17$, respectively. Apart from allowing an estimate of the rotation speed of the star, the presence of multiplets in the frequency spectrum of a pulsating WD can be very useful to identify the harmonic degree of the pulsations. This method to infer the rotation period has been successfully applied to several pulsating WD stars (see Hermes et al. 2017a, for the case of ZZ Ceti stars observed during the *Kepler* and *K2* missions). Winget et al. (1994) detected 10 complete (that is, with all the three components) rotational triplets of frequencies in GD 358 as a result of an intensive scrutiny of this star with the *WET* collaboration. These authors found that the frequency splittings ($\delta\nu$) are not constant, but vary with the radial order, which led them to conclude that the star could be experiencing differential rotation, with the outer envelope rotating some $\sim$ 2 times faster than the core (but see also Kawaler et al. 1999). Kepler et al. (2003) reported the absence of triplets in the 2000 data of GD 358, except for one clear triplet centered at $\sim$ 2154 μHz. Later, Provencal et al. (2009) found only two clear rotational triplets, centered at $\sim$ 2154 μHz and $\sim$ 2363 μHz, and their analysis from 1990 to 2008 revealed a long-term change in the multiplet splittings coinciding with the 1996 *sforzando* event, where the star dramatically altered its pulsation characteristics on a timescale of hours. This phenomena could be attributed to the interaction between convection and/or magnetic fields and pulsations.

The *TESS* data of GD 358 presented in this work reveal the presence of 4 of the 10 triplets found in Winget et al. (1994). At variance with the results of that paper, in the *TESS* data we find two complete triplets and two incomplete triplets. One of the complete triplets has frequencies 2359.010 μHz, 2362.689 μHz, and 2366.318 μHz. Going to smaller frequencies, we find the other complete triplet with frequencies 1623.248 μHz, 1617.409 μHz, and 1611.949 μHz, an incomplete triplet with frequencies 1435.142 μHz and 1421.059 μHz[1], and other incomplete triplet with frequencies 1297.338 μHz and 1289.082 μHz. These rotational triplets are emphasized with boldface in Table 3. We show the rotational triplets in Fig. 3. Similar to the findings of Winget et al. (1994), we find that the frequency splittings $\delta\nu$ in these 4 triplets are not constant, as we will show in Sect. 5.1.

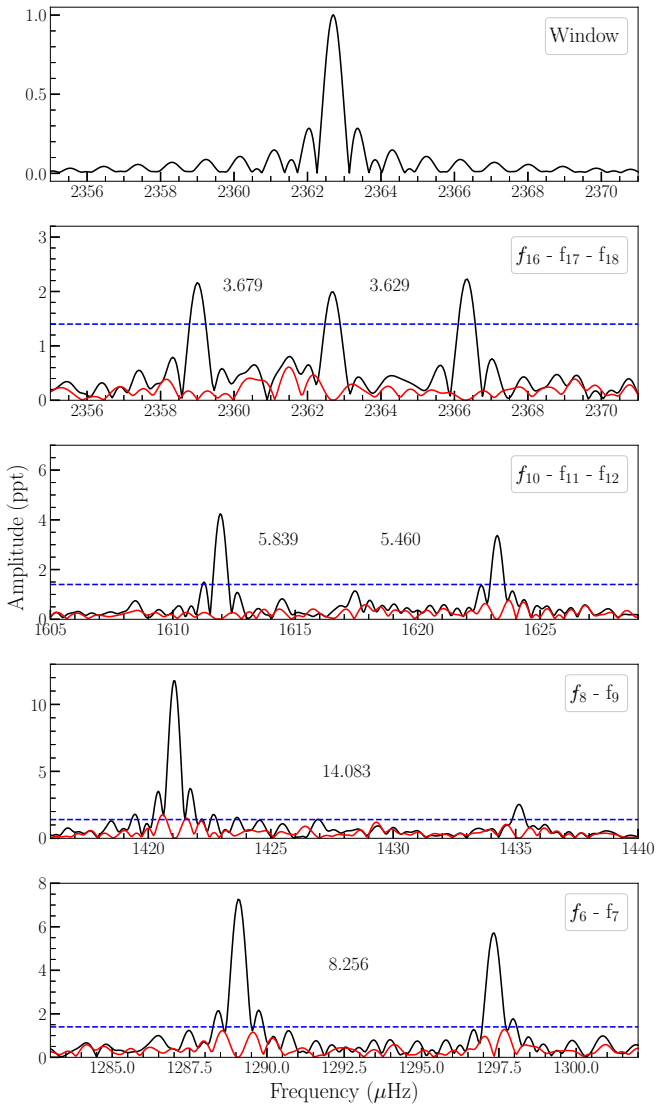

Fig. 3. Rotational triplets in the frequency spectrum of GD 358. The FT are shown with black lines, and residuals with red lines. The blue-dashed horizontal lines correspond to 0.1% FAP confidence levels. The upper panel is the window function.

4. Evolutionary models, numerical codes, and spectroscopic masses

We employ a set of state-of-the-art DB WD stellar models that take into account the complete evolution of the progenitor stars. Specifically, the stellar models were extracted from the evolutionary calculations presented by Althaus et al. (2009) produced with the LPCODE evolutionary code. For details about the input physics and evolutionary code, and the numerical simulations performed to obtain the DB WD evolutionary sequences employed here, we refer the interested reader to that paper. These evolutionary tracks have been employed in the asteroseismic analyses of the DBV stars KIC 8626021 (Córsico et al. 2012), KUV 05134+2605 (Bognár et al. 2014), PG 1351+489 (Córsico et al. 2014), and WD 0158−160 (Bell et al. 2019). The sequences of DB WD models have been obtained taking into account a complete treatment of the evolutionary history of progenitors stars, starting from the zero-age main sequence (ZAMS),

[1] Between these two frequencies there is a frequency of 1426.986 μHz but with a very low amplitude (1.294 ppt), which could be the $m = 0$ component of the triplet, although the splittings of the triplet would be quite different ($\delta\nu \sim 8$ μHz and $\delta\nu \sim 6$ μHz). A peak of similar frequency (1427.27 μHz) has been reported by Winget et al. (1994) with appreciable amplitude (19 ppt). However, we will not include the frequency of 1426.986 μHz in this work since all periods detected in GD 358 from ground-based observations such as those of Winget et al. (1994) are taken into account through the "mean periods" calculated by Bischoff-Kim et al. (2019); see Section 5.1.

Table 3. Identified frequencies (combination frequencies), periods, and amplitudes (and their uncertainties) and the signal-to-noise ratio in the data of GD 358.

Peak	ν (μHz)	Π (s)	A (ppt)	S/N
f_1	919.507 ± 0.018	1087.538 ± 0.021	2.521 ± 0.18	10.5
f_2	1038.177 ± 0.026	963.226 ± 0.025	1.739 ± 0.18	7.2
f_3	1082.770 ± 0.008	923.556 ± 0.007	5.723 ± 0.18	23.8
f_4	1170.146 ± 0.015	854.593 ± 0.011	3.115 ± 0.18	12.9
f_5	1232.928 ± 0.004	811.076 ± 0.003	10.325 ± 0.18	43.0
$\mathbf{f_6}$	1289.082 ± 0.006	775.745 ± 0.003	7.212 ± 0.18	30.0
$\mathbf{f_7}$	1297.338 ± 0.008	770.808 ± 0.005	5.574 ± 0.18	23.2
$\mathbf{f_8}$	1421.059 ± 0.004	703.700 ± 0.002	11.782 ± 0.18	49.0
$\mathbf{f_9}$	1435.142 ± 0.018	696.794 ± 0.009	2.530 ± 0.18	10.5
$\mathbf{f_{10}}$	1611.949 ± 0.010	620.367 ± 0.004	4.327 ± 0.18	18.0
$\mathbf{f_{11}}$	1617.409 ± 0.034	618.272 ± 0.013	1.352 ± 0.18	5.6
$\mathbf{f_{12}}$	1623.248 ± 0.013	616.048 ± 0.005	3.403 ± 0.18	14.1
f_{13}	2024.182 ± 0.020	494.026 ± 0.005	2.280 ± 0.18	9.5
f_{14}	2154.064 ± 0.010	464.238 ± 0.002	4.360 ± 0.18	18.1
f_{15}	2157.584 ± 0.042	463.481 ± 0.009	1.109 ± 0.18	4.6
$\mathbf{f_{16}}$	2359.010 ± 0.021	423.906 ± 0.003	2.214 ± 0.18	9.2
$\mathbf{f_{17}}$	2362.689 ± 0.021	423.246 ± 0.003	2.169 ± 0.18	9.0
$\mathbf{f_{18}}$	2366.318 ± 0.019	422.597 ± 0.003	2.380 ± 0.18	9.9
$2f_1$	1839.301 ± 0.031	543.684 ± 0.009	1.498 ± 0.18	6.2
f_3+f_5	2315.669 ± 0.036	431.840 ± 0.006	1.282 ± 0.18	5.3
$2f_5$	2465.756 ± 0.026	405.555 ± 0.004	1.772 ± 0.18	7.3
f_5+f_7	2530.302 ± 0.034	395.209 ± 0.005	1.337 ± 0.18	5.5
f_5+f_8	2653.958 ± 0.028	376.795 ± 0.004	1.614 ± 0.18	6.7
f_6+f_{12}	2912.290 ± 0.040	343.372 ± 0.004	1.147 ± 0.18	4.7
f_8+f_{12}	3044.295 ± 0.029	328.483 ± 0.003	1.586 ± 0.18	6.6
f_5+f_{14}	3386.984 ± 0.038	295.247 ± 0.003	1.213 ± 0.18	5.0

through the thermally pulsing asymptotic giant branch (TP-AGB) and born-again (VLTP; very late thermal pulse) phases to the domain of the PG 1159 stars, and finally the DB WD stage. As such, they are characterized by evolving chemical profiles consistent with the prior evolution. We varied the stellar mass and the effective temperature in our model calculations, while the He content, the chemical structure at the CO core, and the thickness of the chemical interfaces were fixed by the evolutionary history of progenitor objects. The models employ the ML2 prescription of convection with the mixing length parameter, α, fixed to 1 (Bohm & Cassinelli 1971; Tassoul et al. 1990). Specifically, we considered nine DB WD sequences with stellar masses of: 0.515, 0.530, 0.542, 0.565, 0.584, 0.609, 0.664, 0.741, and $0.870 M_{\odot}$. These DB WD sequences are characterized by the maximum He-rich envelope that can be left by prior evolution if we assume that they are the result of a born-again episode. The value of envelope mass ranges from $M_{\rm He}/M_{*} \sim 2 \times 10^{-2}$ ($M_{*} = 0.515 M_{\odot}$) to $M_{\rm He}/M_{*} \sim 1 \times 10^{-3}$ ($M_{*} = 0.870 M_{\odot}$). In Figure 1 we show the complete set of DB WD evolutionary tracks (with different colors according to the value of the stellar mass) along with the location of all the DBVs known to date (Córsico et al. 2019), including GD 358.

We have employed $\ell = 1, 2$ g-mode pulsation periods in the range 80 – 1500 s computed with the adiabatic and nonadiabatic versions of the pulsation code LP-PUL (Córsico & Althaus 2006; Córsico et al. 2006, 2009) and the same methods employed in the previous works of de La Plata Stellar Evolution and Pulsation Research Group[2].

[2] http://fcaglp.fcaglp.unlp.edu.ar/evolgroup/

On the basis of the evolutionary tracks presented in Fig. 1 and the published values of the spectroscopic surface gravity and temperature, we derive by interpolation a value of the spectroscopic mass of GD 358. This is relevant because this same set of DB WD models is used in the next Section to derive the stellar mass from the period spacing. We get a stellar mass of $M_{\star} = 0.508 \pm 0.050\ M_{\odot}$ if $T_{\rm eff} = 24\,000 \pm 500$ K and $\log g = 7.80 \pm 0.05$ (Nitta et al. 2012), and $M_{\star} = 0.560 \pm 0.028\ M_{\odot}$ if $T_{\rm eff} = 24\,937 \pm 1\,018$ K and $\log g = 7.92 \pm 0.05$ (Bédard et al. 2017). The uncertainties in the stellar mass are estimated from the uncertainties in the $T_{\rm eff}$ and $\log g$ values adopting the extreme values of each parameter when interpolating between the evolutionary tracks of Fig. 1.

5. Asteroseismology

In the asymptotic limit of high-radial orders ($k \gg \ell$), the periods of g modes with consecutive radial order are approximately evenly separated (Tassoul et al. 1990), being the constant period spacing dependent on the harmonic degree:

$$\Delta\Pi_{\ell}^{\rm a} = \frac{\Pi_0}{\sqrt{\ell(\ell+1)}}, \tag{1}$$

Π_0 being a constant value defined as:

$$\Pi_0 = \frac{2\pi^2}{\left[\int_{r_1}^{r_2} \frac{N}{r} dr\right]}, \tag{2}$$

where N is the Brunt-Väisälä frequency. The asymptotic period spacing given by Eq. (1) is very close to the computed period spacing of g modes in chemically homogeneous stellar models without convective regions (Tassoul 1980). In the case of pulsating DB WDs, they may have a surface convective zone, although usually very thin compared to the stellar radius. On the other hand, they have several chemical composition gradients. Mainly for this last reason, the calculated period spacing does not coincide with the asymptotic period spacing given by Eq. (1), but nevertheless the *average* of the calculated spacing is very close to $\Delta\Pi_\ell^{\rm a}$ for radial orders high enough. The departures of the period spacing from the averaged period spacing are provoked by the mechanical resonance called "mode trapping". The presence of one or more narrow regions in which the abundances of nuclear species are rapidly varying strongly modifies the character of the resonant cavity in which modes propagate as standing waves. Specifically, chemical interfaces act like reflecting walls that partially trap certain modes, forcing them to oscillate with larger amplitudes in specific regions – bounded either by two interfaces or by one interface and the stellar center or surface – and with smaller amplitudes outside of those regions. The requirement for a mode to be trapped is that the wavelength of its radial eigenfunction matches the spatial separation between two interfaces or between one interface and the stellar center or surface. Mode trapping has been intensively studied in the context of DAV, DBV, and GW Vir stars (see, e.g., Brassard et al. 1992; Bradley et al. 1993; Kawaler & Bradley 1994; Córsico et al. 2002; Córsico & Althaus 2006).

The methods we use in this paper to extract information of the stellar mass and the internal structure of GD 358 are the same employed in Córsico et al. (2021) for GW Vir stars observed with *TESS* (see, also, Córsico et al. 2012; Bognár et al. 2014; Córsico et al. 2014; Bell et al. 2019). Specifically, we compare the observed period spacing of GD 358 ($\Delta\Pi$) with the asymptotic period spacing ($\Delta\Pi_\ell^{\rm a}$) computed with Eq. (1) at the effective temperature of the star to derive an estimate of the stellar mass. DBV stars generally do not have all of their pulsation modes in the asymptotic regime, so there is usually no perfect agreement between $\Delta\Pi$ and $\Delta\Pi_\ell^{\rm a}$. Therefore, the derivation of the stellar mass using the asymptotic period spacing may not be entirely reliable in DBV stars that pulsate with modes characterized by low and intermediate radial orders, but it gives a good estimate of the stellar mass for stars pulsating with g modes of high radial order (see Althaus et al. 2008, for the case of GW Vir stars). A variation of this approach to infer the stellar mass of DBV stars is to compare $\Delta\Pi$ with the average of the computed period spacings ($\overline{\Delta\Pi_k}$). It is calculated as $\overline{\Delta\Pi_k} = (n-1)^{-1}\sum_k \Delta\Pi_k$, where the "forward" period spacing ($\Delta\Pi_k$) is defined as $\Delta\Pi_k = \Pi_{k+1} - \Pi_k$ (k being the radial order) and n is the number of computed periods laying in the range of the observed periods. This method is more reliable for the estimation of the stellar mass of DBV stars than that described above using $\Delta\Pi_\ell^{\rm a}$ because, provided that the average of the computed period spacings is evaluated at the appropriate range of periods, the approach is valid for the regimes of short, intermediate and long periods as well. When the average of the computed period spacings is taken over a range of periods characterized by high k values, then the predictions of the present method become closer to those of the asymptotic period-spacing approach (Althaus et al. 2008). On the other hand, the present method requires detailed period computations, at variance with the method described above, which does not involve pulsational calculations. Note that both methods for assessing the stellar mass rely on the spectroscopic effective temperature, and the results are unavoidably affected by its associated uncertainty. The methods outlined above take full advantage of the fact that the period spacing of DBV stars primarily depends on the stellar mass and the effective temperature, and very weakly on the thickness of the He envelope (see, e.g., Tassoul et al. 1990)[3].

A powerful approach to disentangle the internal structure of DBV stars is to seek theoretical models that best match the individual pulsation periods. To measure the goodness of the match between the theoretical pulsation periods ($\Pi_{\ell,k}$) and the observed individual periods ($\Pi_i^{\rm o}$), we follow the same procedure as in our previous works:

$$\chi^2(M_\star, T_{\rm eff}) = \frac{1}{N}\sum_{i=1}^{N} \min[(\Pi_{\ell,k} - \Pi_i^{\rm o})^2] \tag{3}$$

where N is the number of observed periods. In order to find the stellar model that best fits the observed periods exhibited by the target star –the "asteroseismological" model– we evaluate the function χ^2 for stellar masses $M_\star = 0.515, 0.530, 0.542, 0.565, 0.584, 0.609, 0.664, 0.741, 0.870 M_\odot$. For the effective temperature, we employ a very fine model grid ($\Delta T_{\rm eff} = 10 - 30$ K). The DB WD model that shows the lowest value of χ^2 is adopted as the best-fit asteroseismological model. Below, we employ the tools described above to extract information of GD 358.

5.1. Period spacing and the seismic mass

Ground-based photometric observations of GD 358 span a period of 34 years. No other DBV star has been studied for such a long period of time, which is why we know the most about this object. A detailed compilation of the observations, that includes archival data from 1982 to 2006, and 1195.2 hr of new observations from 2007 to 2016, has been presented by Bischoff-Kim et al. (2019). Figure 4 of that paper, constructed on the basis of the periods and amplitudes of their Tables 2 and 3, is extremely illustrative of how the periods of pulsation in this star are concentrated in bands with finite widths, rather than discrete periods. Frequencies detected in a given observing season are not found in all observing runs, and most of the detected frequencies are not statistically identical from year to year. Only a few frequencies appear with exactly the same values at various observing runs. A similar phenomenon has been reported for the cool DAV star G 29−38 (Kleinman et al. 1998). Regarding the bands of periods exhibited by GD 358, Bischoff-Kim et al. (2019) find a general increase in their width with decreasing frequency (increasing period), at least until the band at 1238 μHz (807 s). This behaviour could be related to the oscillation of the outer convection zone of the WD during pulsations (Montgomery et al. 2020). Specifically, the oscillation in the base of the convection zone would affect the radial eigenfunction of g modes that have the outer turning point of oscillation located precisely at the base of the outer convection zone.

While the origin of this phenomenon is not entirely clear and deserves further exploration, we note that the existence of finite bands of periods poses a problem for applying the asteroseismological tools, because they require a set of *discrete* observed periods (even with possible uncertainties) that must be

[3] These methods cannot, in principle, be directly applied to DAV stars to infer the stellar mass, for which the period spacing depends simultaneously on $M_\star$, $T_{\rm eff}$ and $M_{\rm H}$ with comparable sensitivity, and this implies the existence of multiple combinations of these three quantities that produce the same spacing of periods.

compared with well-defined periods calculated in stellar models of WDs. To tackle this difficulty, Bischoff-Kim et al. (2019) determined the mean periods for each band to be used in the asteroseismic fits (see their Table 5). In the lower and middle panels of Fig. 4, we show schematically all the periods detected from ground-based observations and the mean periods determined by Bischoff-Kim et al. (2019) for each band, respectively. The amplitude has been arbitrarily set to one to facilitate visualization. The period at 1014.35 s in the middle panel, represented with a dashed red line, is not associated to any specific band, but instead corresponds to a single detection in the 2016 ground-based observations. In the upper panel of Fig. 4 we include the 18 periods detected by *TESS* (Table 3). By comparing the mean periods (middle panel) and the periods detected by *TESS* (upper panel), we note that there are at least 9 periods that coincide between both sets, at ∼ 420 s, ∼ 465 s, ∼ 495 s, ∼ 620 s, ∼ 700 s, ∼ 770 s, ∼ 810 s, ∼ 855 s, and ∼ 970 s. Other periodicities are present in the ground-based mean periods but not in the *TESS* periods (∼ 540 s, ∼ 575 s, ∼ 660 s, ∼ 730 s, ∼ 902 s, ∼ 1015 s, and ∼ 1063 s), and vice versa (∼ 925 s and ∼ 1090 s). In order to extract as much information as possible with the tools of asteroseismology, it is crucial to employ as many periods (which represent eigenvalues of the star) as possible. Thus, in order to identify the pulsation modes and determine the possible period spacing of GD 358, which is essential to estimate the stellar mass, we consider an expanded list of periods by adding the 15 dipole $m = 0$ mean periods found by Bischoff-Kim et al. (2019) to the list of periods collected by *TESS* (Table 3). In the case of the 9 periods close to each other detected in both data sets, we decided to adopt the periods measured by *TESS* because they are in general more accurate. In the case of the periods near 700 s, we adopt the period 699.82 s from Bischoff-Kim et al. (2019), which seems to be the central component of the incomplete rotational triplet $(+1, 0, -1)$ = (696.794 s, ..., 703.700 s) detected by *TESS* (see below). The resulting extended list of periods to be used in our analysis contains 26 periods and is shown in the first and second columns of Table 4. Note that we have also considered the period 1014.35 s, which has been detected only in the observations of 2016. This period was not considered in the asteroseismological analysis of Bischoff-Kim et al. (2019). However, since its value seems to fit very well in the apparent pattern of dipole periods with constant separation present in this star, as can be guessed from Fig. 4, we decided to include it in our subsequent analysis.

In the case of the rotational triplets, we have assigned the m value to the different components following Winget et al. (1994). We note that the frequency splittings are not constant among the different triplets. In fact, we have $\delta\nu = 3.679$ μHz and $\delta\nu = 3.629$ μHz for the complete triplet centered at 2362.689 μHz (423.246 s), $\delta\nu = 5.839$ μHz and $\delta\nu = 5.460$ μHz for the complete triplet centered at 1617.409 μHz (618.272 s), $2\,\delta\nu = 14.083$ μHz (that is, $\delta\nu = 7.042$ μHz) for the incomplete triplet with side components 1435.142 μHz (696.794 s) and 1421.059 μHz (703.700 s), and $\delta\nu = 8.256$ μHz for the incomplete triplet centered at 1289.082 μHz (775.745 s). There is an apparent trend of larger $\delta\nu$ for decreasing frequencies (increasing periods), in agreement with Winget et al. (1994) (see their Fig. 6 and Table 2). This dependence of the frequency splittings with the radial order of the modes could indicate differential rotation of GD 358, since each mode samples areas of different depth in the star, and would indicate different speeds of rotation[4]. While these results would imply that GD 358 does not rotate as a rigid body, in order to put this results on a firm basis it would be necessary to make a detailed analysis such as that carried out by Kawaler et al. (1999) (see, also, Córsico et al. 2011, for the specific case of the GW Vir star PG 122+200), which is beyond the scope of this paper.

Table 4. Enlarged list of periods of GD 358. Column 1 corresponds to seven $\ell = 1$ $m = 0$ average periods derived by Bischoff-Kim et al. (2019) (BK19). We include also the period at 1014.35 s extracted from the ground based observations of 2016 (see Table 3 of Bischoff-Kim et al. 2019). Column 2 corresponds to 18 periods detected by *TESS* (Table 3). The periods with an asterisk are the 13 periods used in the linear least square fit depicted in Fig. 6.

$\Pi_i^{\rm O}$ (s) BK19	$\Pi_i^{\rm O}$ (s) *TESS*	$\Pi_{\rm fit}$ (s)	$\delta\Pi$ (s)	$\ell^{\rm O}$	$m^{\rm O}$
	422.597			1	+1
	423.246*	421.697	1.549	1	0
	423.906			1	−1
	463.481*	460.942	2.539	1	0
	464.238			?	?
	494.026			?	?
538.30*		539.433	−1.133	1	0
574.22*		578.678	−4.458	1	0
	616.048			1	+1
	618.272*	617.923	0.349	1	0
	620.367			1	−1
658.69*		657.168	1.522	1	0
	696.794			1	+1
699.82*		696.414	3.406	1	0
	703.700			1	−1
730.28*		735.659	−5.379	1	0
	770.808			1	+1
	775.745*	774.904	0.841	1	0
	811.076*	814.149	−3.073	1	0
	854.593*	853.394	1.199	1	0
901.49				?	?
	923.556			?	?
	963.226			?	?
1014.35*		1010.575	3.775	1	0
1062.32				?	?
	1087.538*	1088.866	−1.328	1	0

We looked for a constant period spacing in the data of GD 358 using the Kolmogorov-Smirnov (K-S; Kawaler 1988), and the inverse variance (I-V; O'Donoghue 1994) significance tests. In the K-S test, the quantity Q is defined as the probability that the observed periods are randomly distributed. Thus, any uniform or at least systematically non-random period spacing in the period spectrum of the star will appear as a minimum in Q. In the I-V test, a maximum of the inverse variance will indicate a constant period spacing.

Fig. 5 displays the results of applying the K-S and I-V significance tests to the set of 26 periods of Table 4. We have considered four situations. In one case, we adopted the full set of 352 periods of Tables 2 and 3 of Bischoff-Kim et al. (2019) (blue curves). In a second case, we adopted the mean periods of Table 5 of Bischoff-Kim et al. (2019) (red curves). We considered also the case of the set of 18 periods measured by *TESS* (black curves). Finally, we considered the case of the *TESS* periods plus the mean periods of Bischoff-Kim et al. (2019) (green curves). In this last case we also considered the period at 1014.35 s disregarded in that paper. The curves have been arbitrarily shifted

[4] We note that it makes no sense to calculate different rotational periods for GD 358 using the different frequency splittings using an uniform-rotation formula like the one described in Sect. 3.

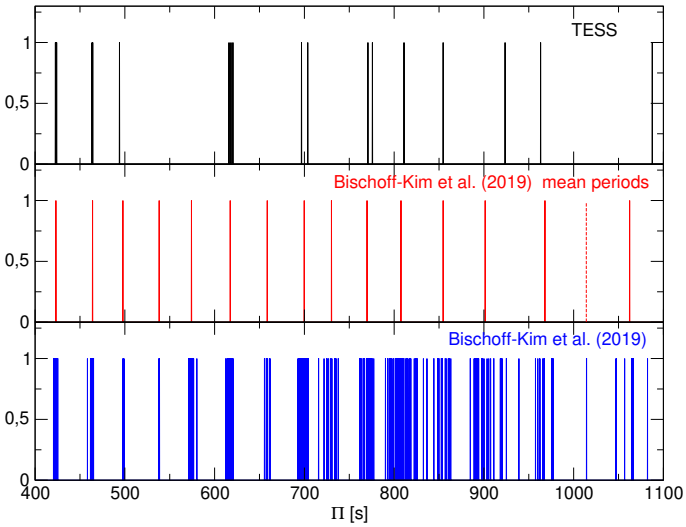

Fig. 4. Schematic distribution of the pulsation periods of GD 358 according to *TESS* (19 periods, black lines, upper panel), and according to Bischoff-Kim et al. (2019) (15 mean periods, red lines, middle panel, and 352 periods, blue lines, lower panel). The period at 1014.35 s in the middle panel, represented with a dashed red line, corresponds to a single detection in the 2016 ground-based observations. The amplitudes have been arbitrarily set to one for clarity.

horizontally for the purpose of better visualization. The two tests point to the existence of a pattern of $\ell = 1$ constant period spacing of $\Delta\Pi \sim 39$ s.

To derive a refined value of the period spacing, we have carried out a linear least-squares fit to the 13 periods marked with an asterisk in Table 4 (see Fig. 6). These periods are all supposed to be the $\ell = 1$ $m = 0$ members of a sequence of periods equally spaced. We obtain a period spacing of $\Delta\Pi = 39.2452 \pm 0.1739$ s. This value is somewhat lower than the period spacing derived by Bischoff-Kim et al. (2019) on the basis of ground-based observations alone ($\Delta\Pi = 39.9$ s). This period spacing corresponds to our expectations for a dipole ($\ell = 1$) sequence. On the other hand, if we assume that the $\sim$ 39 s period spacing were due to quadrupole modes, then the dipole period spacing would be $\sim$ 68 s, which is not present in the tests[5]. Thus, the identification of the $\sim$ 39 s period spacing as due to a sequence of dipole modes is robust. This sequence includes the 13 periods marked with an asterisk in Table 4, and the 7 periods that are the $m = -1$ or $m = +1$ components of the four triplets. The remaining 6 periods in that table can be associated with $\ell = 1$ modes which, due to mode trapping effects, deviate substantially from the derived sequence of almost equally-spaced periods, or with modes with $\ell = 2$ (or possibly higher) modes. In short, we have a total of 20 periods identified with $\ell = 1$ modes. The relevance of finding a constant period spacing is twofold: on the one hand, it enables us to estimate the stellar mass. On the other hand, it enables the identification of the harmonic degree of numerous modes, which simplifies the analysis of period-to-period fits (Sect. 5.2).

In the lower panel of Fig. 6 we show the residuals ($\delta\Pi$) between the dipole observed periods ($\Pi_i^{\rm O}$) and the periods derived from the mean period spacing ($\Pi_{\rm fit}$). The average of the absolute values of the residuals is $\overline{|\delta\Pi|} = 2.35$ s. The presence of several minima in the distribution of residuals strongly suggests the mode-trapping effects inflicted by the presence of internal chemical transition regions.

For this star, we calculated the average of the computed period spacings for $\ell = 1$, $\overline{\Delta\Pi_k}$, in terms of the effective temperature for all the masses considered and a period interval of 400 – 1100 s. The results are shown in Fig. 7, where we depict $\overline{\Delta\Pi_k}$ with curves of different colors according to the various stellar masses. The location of GD 358 is indicated by a small red circle with error bars if we consider the effective temperature derived by Bédard et al. (2017), and by a small black circle when we adopt the $T_{\rm eff}$ inferred by Koester et al. (2014). The period spacing is $\Delta\Pi = 39.2452 \pm 0.1739$ s. We perform linear interpolations and obtain $M_\star = 0.605 \pm 0.023\, M_\odot$ (if $T_{\rm eff} = 24\,000$ K), and $M_\star = 0.581 \pm 0.031\, M_\odot$ (if $T_{\rm eff} = 24\,937$ K). We note that the spectroscopic mass assuming the high $T_{\rm eff}$ is slightly smaller than, but in very good agreement with, the mass derived from the period spacing for that $T_{\rm eff}$ (0.560 vs $0.581 M_\odot$). At variance with this, the spectroscopic mass assuming the low $T_{\rm eff}$ ($M_\star \sim 0.508 M_\odot$) is substantially lower ($\sim$ 20%) than the mass derived from the period spacing for that $T_{\rm eff}$ ($M_\star \sim 0.605 M_\odot$). We conclude that the period spacing of GD 358 seems to favour the spectroscopic determination of $T_{\rm eff}$ and $\log g$ of Bédard et al. (2017).

5.2. Period fits and the asteroseismological model

Next, we describe our period-to-period fit procedure. In our analysis of period-to-period fits, we only considered the components $m = 0$ present in the frequency spectrum of GD 358, and ignore the $m \neq 0$ components. In total we, have 19 observed periods as the input for our asteroseismological period fits (see column 1 of Table 5). Following the results obtained in Sect. 5.1, we assume that a subset of 13 $m = 0$ periods are associated with $\ell = 1$ modes — those marked with an asterisk in Table 4— and leave free the assignment as $\ell = 1$ or $\ell = 2$ for the remaining 6 periods. We display our results in Fig. 8. We find three possible solutions, that is, maxima of $(\chi^2)^{-1}$, labelled as (1), (2), and (3), which are compatible with both effective temperature determinations of GD 358 and its uncertainties. These solutions are (1) $T_{\rm eff} = 24\,967$ K and $M_\star = 0.584\ M_\odot$ ($\chi^2 = 9.921$), (2) $T_{\rm eff} = 25\,712$ K and $M_\star = 0.565\ M_\odot$ ($\chi^2 = 11.758$), and (3) $T_{\rm eff} = 24\,240$ K and $M_\star = 0.609\ M_\odot$ ($\chi^2 = 17.595$). Clearly, the optimal solution is (1), since the DB WD model associated to it provides the best agreement between the theoretical and observed periods. Note that the effective temperature of this model is very close to that of GD 358 according to the spectroscopic determination of Bédard et al. (2017).

We adopt the model characterized by $M_\star = 0.584 M_\odot$, $T_{\rm eff} = 24\,967$ K, and $\log(L_\star/L_\odot) = -1.215$ as the asteroseismological model for GD 358. The location of this model in the $\log g - T_{\rm eff}$ diagram is displayed in Fig. 1 with a blue circle. In Table 5 we show a detailed comparison of the observed periods of GD 358 and the theoretical $m = 0$ periods of the asteroseismological model. According to this model, the periods exhibited by the star correspond to 16 dipole $m = 0$ modes with radial order k in the range $k \in [8, 25]$, and 3 quadrupole modes with $36 \leq k \leq 43$. The average of the dipole computed period spacings for this model is $\overline{\Delta\Pi}_{\ell=1} = 38.926$ s, very close to the dipole mean period spacing derived in Sect. 5.1 for this star, $\Delta\Pi = 39.2452 \pm 0.1739$ s. In order to quantitatively assess the quality of our period fit, we compute the average of the absolute period differences, $\overline{\delta\Pi_i} = \left(\sum_{i=1}^{n} |\delta\Pi_i|\right)/n$, where $\delta\Pi_i = (\Pi_{\ell,k} - \Pi_i^{\rm o})$ and $n = 19$, and

[5] If such a dipole period spacing of $\sim$ 68 s existed, it would involve an extremely low stellar mass for GD 358, which can safely be ruled out.

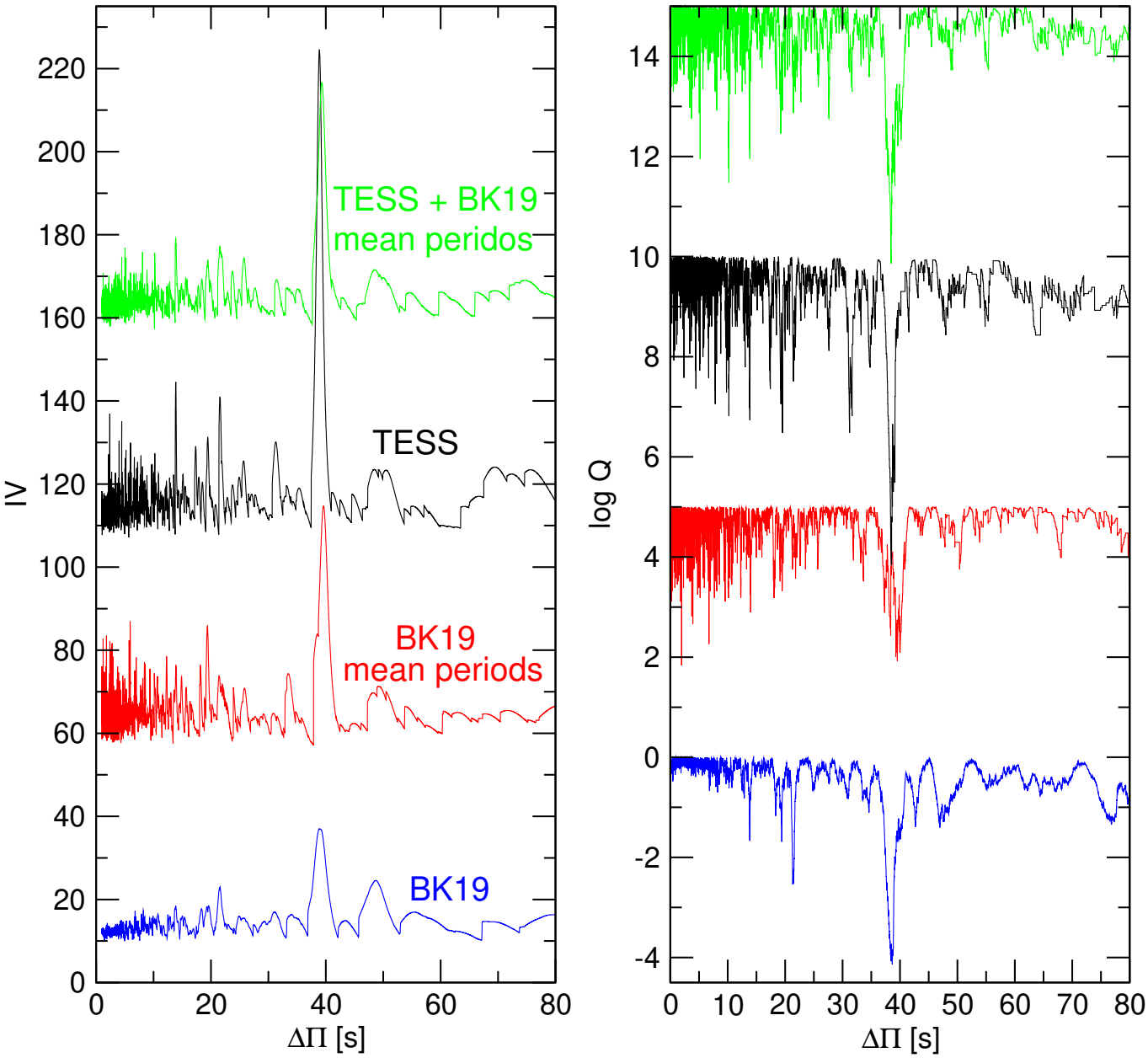

Fig. 5. I-V (left panel) and K-S (right panel) significance tests to search for a constant period spacing in GD 358. The tests are applied to the complete set of 352 pulsation periods of Tables 2 and 3 of Bischoff-Kim et al. (2019) (blue curves), the set of mean periods of Table 5 of Bischoff-Kim et al. (2019) plus the period at 1014.35 s (red curves), the list of *TESS* periods (black curves) of Table 3, and the combination of the *TESS* periods plus the mean periods of Bischoff-Kim et al. (2019) (green curves), included in Table 4. A clear signal of a constant period spacing at ∼ 39 s is evident. See text for details.

the root-mean-square residual, $\sigma = \sqrt{(\sum_{i=1}^{n} |\delta\Pi_i|^2)/n} = \sqrt{\chi^2}$. We obtain $\overline{\delta\Pi_i} = 2.56$ s and $\sigma = 3.15$ s. In order to have a global indicator of the goodness of the period fit that takes into account the number of free parameters, the number of fitted periods, and the proximity between the theoretical and observed periods, we computed the Bayes Information Criterion (BIC; Koen & Laney 2000):

$$\mathrm{BIC} = n_{\mathrm{p}} \left(\frac{\log N}{N} \right) + \log \sigma^2, \tag{4}$$

where n_{p} is the number of free parameters of the models, and N is the number of observed periods. The smaller the value of BIC, the better the quality of the fit. In our case, $n_{\mathrm{p}} = 2$ (stellar mass and effective temperature), $N = 19$, and $\sigma = 3.15$ s. We obtain BIC = 1.13, which means that our period fit is good.

We also include in Table 5 the rates of period change ($\dot{\Pi} \equiv d\Pi/dt$) predicted for each g mode of GD 358. Note that all of them are positive ($\dot{\Pi} > 0$), implying that the periods are lengthening over time. The rate of change of periods in WDs and pre-WDs is related to $\dot{T}$ (T being the temperature at the region of the period formation) and $\dot{R}_\star$ ($R_\star$ being the stellar radius) through the order-of-magnitude expression $(\dot{\Pi}/\Pi) \approx -a\,(\dot{T}/T) + b\,(\dot{R}_\star/R_\star)$ (Winget et al. 1983a). According to our asteroseismological model, the star is cooling with approximately constant stellar radius. As a consequence, $\dot{T} < 0$ and $\dot{R}_\star \sim 0$, and then, $\dot{\Pi} > 0$. Can we compare these theoretical estimates of the secular drift of the periods with the true rates of period change

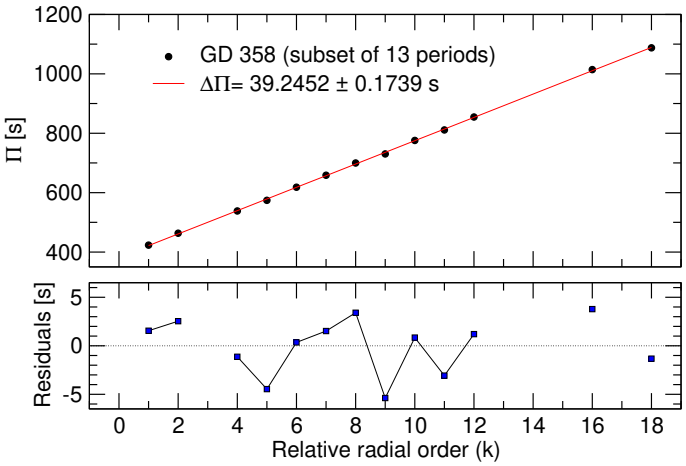

Fig. 6. Upper panel: linear least-squares fit to the 13 periods of GD 358 marked with asterisks in Table 4. The derived period spacing from this fit is $\Delta\Pi = 39.2452 \pm 0.1739$ s. Lower panel: the residuals of the period distribution relative to the mean period spacing, revealing signals of mode trapping in the period spectrum of GD 358. Modes with consecutive radial order are connected with thin black lines.

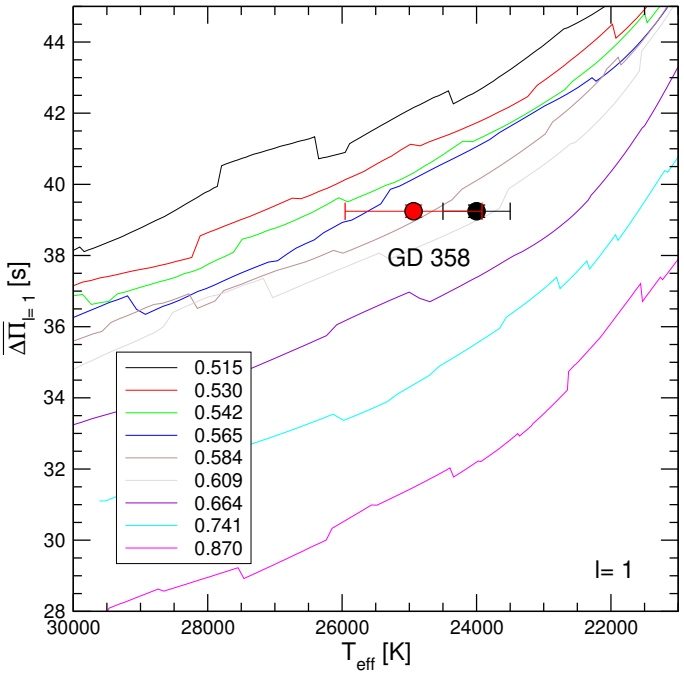

Fig. 7. Dipole ($\ell = 1$) average of the computed period spacings, $\overline{\Delta\Pi_k}$, assessed in a range of periods that includes the periods observed in GD 358, shown as curves of different colors according to the different stellar masses. We consider the two possible effective temperatures for the star, that is, $T_{\rm eff} = 24\,000 \pm 500$ K (black circle; Koester et al. 2014) and $T_{\rm eff} = 24\,937 \pm 1\,018$ K (red circle; Bédard et al. 2017), and the period spacing $\Delta\Pi = 39.2452 \pm 0.1739$ s derived in Sect. 5.1. We include the error bars associated to the uncertainties in $\overline{\Delta\Pi_k}$ and $T_{\rm eff}$. The stellar mass derived by interpolation is $M_\star = 0.605 \pm 0.023 M_\odot$ or $M_\star = 0.581 \pm 0.031 M_\odot$, according to the $T_{\rm eff}$ we adopt.

of GD 358? The frequencies (periods) 2362.689 μHz (423.246 s) and 2154.064 μHz (464.238 s) of GD 358, corresponding to the g modes with $k = 8$ and $k = 9$ according to our asteroseismological model, are the most stable frequencies of this star (Kepler et al. 2003; Provencal et al. 2009). However, the frequency shifts are large enough to mask any possible signs of evolutionary period change. Thus, we are forced to conclude that the observed periods of GD 358 are not stable enough to be able to measure the rate of change of periods due to the evolution of the star. This means that the values derived for the rate of change of periods of our seismological model of GD 358 remain (for now) only of academic interest.

We have also examined the pulsational stability/instability nature of the modes associated with the periods fitted to the observed ones according our asteroseismological model. We assume the frozen-in convection approximation (Unno et al. 1989). In particular, we examine the sign and magnitude of the linear nonadiabatic growth rates, $\eta_k = -\Im(\sigma_k)/\Re(\sigma_k)$, where $\Re(\sigma_k)$ and $\Im(\sigma_k)$ are the real and the imaginary parts, respectively, of the complex eigenfrequency σ_k. A positive value of η_k means that the mode is linearly unstable (eight column of Table 5). In the left (right) hand panel of Fig. 9, we show the instability domain of $\ell = 1$ ($\ell = 2$) periods in terms of the effective temperature for the DB WD model sequence with $M_\star = 0.584 M_\odot$. The palette of colors (right hand scale) indicates the value of the logarithm of the e-folding time, τ_e (in years) of each unstable mode, being $\tau_e = 1/|\Im(\sigma_k)|$. As can be seen, many unstable pulsation modes exist, and interestingly, the interval of periods corresponding to unstable modes of our asteroseismological model is almost coincident with the range of excited periods in GD 358 for most of the range of allowed effective temperatures. In particular, the pulsation periods of GD 358 fall into the highest excitation regimen (that is, shortest e-folding times), which reflects an excellent agreement between our nonadiabatic calculations and the observational data.

In Table 7, we list the main characteristics of GD 358 according to the previous studies and the present work. Most of the data of this table are extracted from Table 7 of Bischoff-Kim et al. (2019). In the case of the results of the present work, the errors in $T_{\rm eff}$ and $\log(L_\star/L_\odot)$ are estimated from the width of the maximum in the function $(\chi^2)^{-1}$ vs $T_{\rm eff}$ and $\log(L_\star/L_\odot)$, respectively, and the error in the stellar mass comes from the grid resolution in $M_\star$. Errors in the remainder quantities, $\log g$ and $\log(R_\star/R_\odot)$, are derived from these values. The seismological stellar mass ($0.584^{+0.025}_{-0.19} M_\odot$) is somewhat larger than the values derived from spectroscopy, although still compatible with them ($0.508 \pm 0.050 M_\odot$ and $0.560 \pm 0.028 M_\odot$) within their uncertainties. In addition, the stellar mass of the asteroseismological model is in excellent agreement with the stellar mass values derived from the mean period spacing ($0.605 \pm 0.023 M_\odot$, and $0.581 \pm 0.031 M_\odot$). We can conclude that the three approaches to determine stellar mass of GD 358 give very similar results, which implies that it is a well-constrained quantity.

In comparison with previous seismological studies, the effective temperature of our asteroseismological model is the largest one, although very similar to that derived by Fontaine & Brassard (2002), and in excellent agreement with the spectroscopic $T_{\rm eff}$ inferred by Bédard et al. (2017). Regarding the stellar mass of our asteroseismological model, its value is in excellent agreement with the values derived in all previous studies. Direct comparison of other quantities such as the central abundance of O ($X_{\rm O}$), the thickness of the envelope rich in O, C, and He, $\log(1 - M_{\rm env}/M_\star)$, or the thickness of the pure helium envelope, $\log(1 - M_{\rm He}/M_\star)$, becomes less clear because the chemical structure of our DB WD models is (by construction) substantially different from those used in previous studies. Even so, we can note that the envelope of our asteroseismological model is somewhat

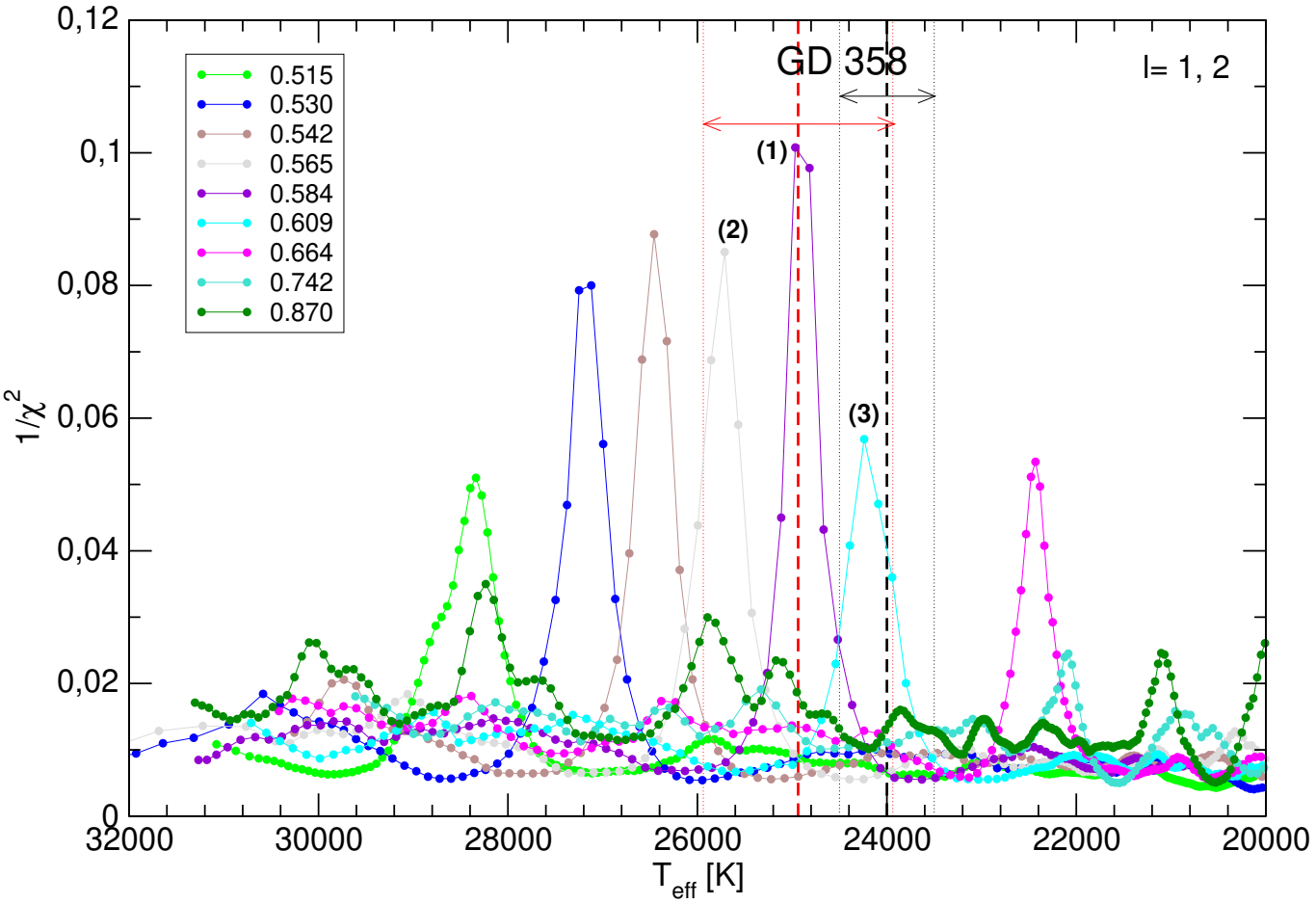

Fig. 8. The inverse of the quality function of the period fit in terms of the effective temperature, depicted with different colors according to the various stellar masses. The vertical black dashed line indicates the spectroscopic $T_{\rm eff}$ of GD 358 and the vertical dotted lines its uncertainties according to Koester et al. (2014) ($T_{\rm eff}$ = 24 000 ± 500 K). Similarly, the blue vertical lines correspond to the spectroscopic $T_{\rm eff}$ and its uncertainties as derived by Bédard et al. (2017) ($T_{\rm eff}$ = 24 937 ± 1 018 K). Three maxima have been labeled as (1), (2) and (3), corresponding to the three asteroseismological solutions compatible with spectroscopy (see the text).

Table 5. Observed and theoretical $m = 0$ periods of the asteroseismological model for GD 358 [$M_\star = 0.584 M_\odot$, $T_{\rm eff}$ = 24 967 K, $\log(L_\star/L_\odot) = -1.215$] corresponding to solution (1) in Fig. 8. $\delta\Pi_k = \Pi_i^{\rm O} - \Pi_k$ represents the period differences, ℓ the harmonic degree, and k the radial order. The last column gives information about the pulsational stability/instability nature of the modes.

$\Pi_i^{\rm O}$ (s)	$\ell^{\rm O}$	Π_k (s)	ℓ	k	$\delta\Pi_k$ (s)	$\dot{\Pi}_k$ (10^{-13} s/s)	Unstable
423.246	1	420.975	1	8	2.272	0.725	yes
463.481	1	462.511	1	9	0.970	1.354	yes
464.238	?	462.511	1	9	1.727	1.354	yes
494.026	?	499.054	1	10	−5.028	1.146	yes
538.300	1	538.126	1	11	0.174	1.394	yes
574.220	1	572.947	1	12	1.273	1.041	yes
618.272	1	617.647	1	13	0.625	1.319	yes
658.690	1	657.517	1	14	1.173	1.735	yes
699.820	1	696.097	1	15	3.723	1.650	yes
730.280	1	732.797	1	16	−2.517	1.506	yes
775.745	1	770.251	1	17	5.494	1.621	yes
811.076	1	812.662	1	18	−1.586	2.014	yes
854.593	1	853.775	1	19	0.818	2.026	yes
901.490	?	894.617	2	36	6.873	2.176	yes
923.556	?	926.073	1	21	−2.517	1.900	yes
963.226	?	965.149	2	39	−1.923	2.704	yes
1014.350	1	1010.499	1	23	3.851	2.470	yes
1062.320	?	1063.670	2	43	−1.350	3.004	yes
1087.538	1	1082.719	1	25	4.819	2.420	yes

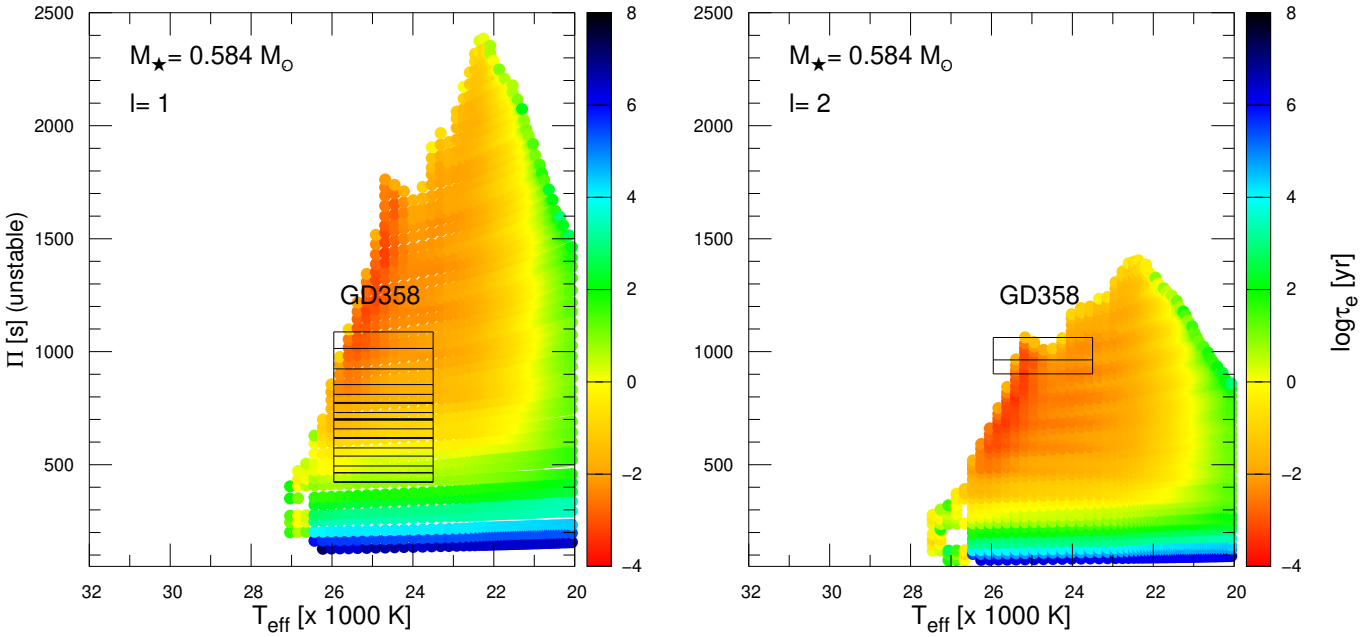

Fig. 9. Left panel: periods of unstable $\ell = 1$ g modes in terms of the effective temperature, with the palette of colors (right scale) indicating the value of the logarithm of the e-folding time (τ_e in years), corresponding to the DB WD sequence with $M_\star = 0.584 M_\odot$. Right panel: same as left panel, but for $\ell = 2$ modes. In both panels, the pulsation periods of the DBV star GD 358 with the identification of ℓ according to our asteroseismological model (see Table 5), are shown as horizontal segments, where their widths represent the possible $T_{\rm eff}$ interval, according to spectroscopy.

Table 7. The main characteristics of the DBV star GD 358. The second column corresponds to spectroscopic and astrometric results, whereas the third, fourth, fifth, sixth, seventh, and eighth columns present the results from the seismological studies of BW94 (Bradley & Winget 1994), DK95 (Dehner & Kawaler 1995), MEA00 (Metcalfe et al. 2000), MEA01 (Metcalfe et al. 2001), FB02 (Fontaine & Brassard 2002), M03 (Metcalfe 2003), and BKEA19 (Bischoff-Kim et al. 2019), respectively, and the last column presents the seismological results from the present work.

Quantity	Spectroscopy Astrometry	BW94	DK95	MEA00	MEA01	FB02	M03	BKEA19	Seismology (this work)
$T_{\rm eff}$ [K]	$24\,000 \pm 500^{(a)}$ $24\,937 \pm 1018^{(b)}$	24 000	24 121	22 600	22 600	24 800	22 900	23 650	$24\,967 \pm 200$
$\log g$ [cm/s^2]	$7.78 \pm 0.05^{(a)}$ $7.92 \pm 0.05^{(b)}$	8.0	···	···	···	8.02	···	···	$7.964^{+0.048}_{0.043}$
$M_\star$ [$M_\odot$]	$0.508 \pm 0.050^{(c)}$ $0.560 \pm 0.028^{(d)}$	0.61	0.58	0.605	0.65	0.625	0.66	0.571	$0.584^{+0.025}_{-0.019}$
$\log(L_\star/L_\odot)$	···	−1.30	···	···	···	−1.25	···	−1.287	-1.215 ± 0.015
$\log(R_\star/R_\odot)$	···	−1.90	···	···	···	−1.89	···	···	-1.880 ± 0.014
$X_{\rm O}$ (center)	···	0.50	0.50	0.80	0.84	0.00	0.67	0.50	0.77
$\log(1 - M_{\rm env}/M_\star)$	···	···	−2.6	−2.74	−2.74	−2.97	···	−2	−1.6
$\log(1 - M_{\rm He}/M_\star)$	···	−5.70	−6.0	−5.97	···	−5.80	−2.0	−5.5	−5.98
d [pc]	$36.6 \pm 4.5^{(b)}$ $43.02 \pm 0.04^{(e)}$	42	···	···	···	43	···	44.5	42.85 ± 0.73

References: (a) Nitta et al. (2012); (b) Bédard et al. (2017); (c) From the evolutionary tracks and the $T_{\rm eff}$ and $\log g$ values of Nitta et al. (2012); (d) From the evolutionary tracks and the $T_{\rm eff}$ and $\log g$ values of Bédard et al. (2017); (e) *Gaia*.

thicker than in the previous studies, and that the pure-He envelope has a thickness quite similar to the thickness derived in other works.

We briefly describe the main properties of our asteroseismological DB model for GD 358. We show in Fig. 10 the internal chemical structure of this model (upper panel), where the abundance by mass of the main constituents (^{4}He, ^{12}C, and ^{16}O) is shown in terms of the outer mass fraction $[-\log(1 - M_r/M_\star)]$. The chemical structure of the model consists of a C/O core – resulting from the core He burning of the previous evolution– shaped by processes of additional mixing, for example, overshooting. The core is surrounded by a mantle rich in He, C, and O, which is the remnant of the regions altered by the nucleosynthesis during the thermally pulsing asymptotic giant branch. Above this shell, there is a pure He mantle constructed by the action of gravitational settling that causes He to float to the surface and heavier species to sink. The lower panel of Fig. 10 displays the run of the squares of the two critical frequencies of nonradial stellar pulsations, that is, the Brunt-Väisälä frequency and the Lamb frequency L_ℓ for $\ell = 1$ and $\ell = 2$. The precise shape of the Brunt-Väisälä frequency largely determines the properties of the g-mode period spectrum of the model. In particular,

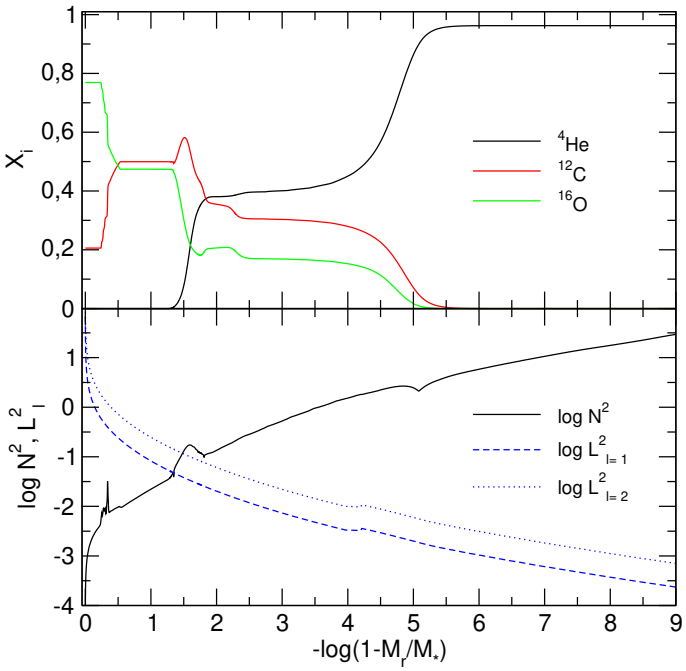

Fig. 10. Internal chemical structure (upper panel) and the squared Brunt-Väisälä and Lamb frequencies for $\ell = 1$ and $\ell = 2$ (lower panel) corresponding to our asteroseismological DB WD model with a stellar mass $M_\star = 0.584 M_\odot$ and an effective temperature $T_{\rm eff} = 24\,967$ K.

each chemical gradient in the model contributes locally to the value of N. The most notable feature is the highly peaked structure at the C/O chemical transition [$-\log(1 - M_r/M_\star) \sim 0.34$]. On the other hand, there is the He/C/O transition region at $-\log(1-M_r/M_\odot) \sim 1.3-1.8$ that produces a notable bump in the Brunt-Väisälä frequency and affect the mode-trapping properties of the model.

5.3. Asteroseismological distance

We can estimate an asteroseismological distance to GD 358 on the basis of the luminosity of the asteroseismological model [$\log(L_\star/L_\odot) = -1.215 \pm 0.015$ and $T_{\rm eff} = 24\,967 \pm 200$ K] and a bolometric correction $BC = -2.71$ (Bradley & Winget 1994). The absolute magnitude can be assessed as $M_{\rm V} = M_{\rm B} - BC$, where $M_{\rm B} = M_{\rm B,\odot} - 2.5\ \log(L_\star/L_\odot)$. We employ the solar bolometric magnitude $M_{\rm B\odot} = 4.74$ (Cox 2000). The seismological distance d is derived from the relation: $\log d = [m_{\rm V} - M_{\rm V} + 5]/5$. We use the apparent visual magnitude $m_{\rm V} = 13.65 \pm 0.01$ (Winget et al. 1982a), and obtain the seismological distance and parallax $d = 42.85 \pm 0.73$ pc and $\pi = 23.33 \pm 0.41$ mas. The uncertainty in the seismological distance comes from the uncertainty in the luminosity of the asteroseismological model. These values are consistent with the results of Bradley & Winget (1994) and Bischoff-Kim et al. (2019), although a bit larger than the distance derived by Bédard et al. (2017). A very important check for the validation of the asteroseismological model is the comparison of the seismological distance with the distance derived from astrometry. We have available the estimates from *Gaia* EDR3, $d_{\rm G} = 43.02 \pm 0.04$ pc and $\pi_{\rm G} = 23.244 \pm 0.024$ mas. They are in excellent agreement with the asteroseismological derivations. This adds robustness to the asteroseismological model we found for GD 358. Also, the match of seismological and trigonometric parallax confirm that we are seeing dipole modes.

6. Summary and conclusions

In this paper, we have presented new *TESS* observations of the already known DBV star GD 358, and carried out a detailed asteroseismological analysis employing fully evolutionary models of DB WDs. The present study is the third part of a series of papers devoted to the study of pulsating H-deficient WDs observed with *TESS*. We extracted 24 periodicities from the *TESS* light curve of GD 358 using a standard pre-whitening procedure to derive the potential pulsation frequencies. The oscillation frequencies, associated to g-mode pulsations, have periods from $\sim$ 295 s to $\sim$ 1087 s. We combined these space data with the abundant ground-based observations available and found a constant period spacing of 39.25 ± 0.17 s, which allowed us to infer its stellar mass ($M_\star = 0.581 \pm 0.031 M_\odot$) and constrain the harmonic degree ℓ of some of the modes. We performed a period-to-period fit analysis on GD 358, which provides us with an asteroseismological model with a stellar mass ($M_\star = 0.584^{+0.025}_{-0.019} M_\odot$) in agreement with the stellar-mass value inferred from the period spacing, and also compatible with the spectroscopic mass ($M_\star = 0.560 \pm 0.028 M_\odot$). In agreement with previous works, we found that the frequency splittings vary according to the radial order of the modes, suggesting differential rotation and preventing us to derive a reliable representative rotation period of the star. The seismological model derived from our analysis allowed us to estimate the seismological distance ($d_{\rm seis} = 42.85 \pm 0.73$ pc) of GD 358, which is in excellent agreement with the precise astrometric distance measured by *GAIA* EDR3 ($d_{\rm GAIA} = 43.02 \pm 0.04$ pc).

In accordance with the findings of our recent works focused on pulsating H-deficient WDs (Bell et al. 2019; Córsico et al. 2021; Uzundag et al. 2021) we conclude that the high-quality data collected by the *TESS* space mission, combined with ground-based photometric data, are able to provide a reliable input to the asteroseismology of WD stars. The *TESS* mission, along with future space missions and upcoming surveys, will allow an unprecedented boost to the stellar seismology of these ancient stars.

Acknowledgements. Part of this work was supported by AGENCIA through the Programa de Modernización Tecnológica BID 1728/OC-AR, and by the PIP 112-200801-00940 grant from CONICET. M.U. acknowledges financial support from CONICYT Doctorado Nacional in the form of grant number No: 21190886 and ESO studentship program. K.J.B. is supported by the National Science Foundation under Award AST-1903828. S.O.K. acknowledges financial support from Coordenação de Aperfeiçoamento de Pessoal de Nível Superior - Brasil (CAPES) - Finance Code 001, Conselho Nacional de Desenvolvimento Científico e Tecnológico - Brasil (CNPq), and Fundação de Amparo à Pesquisa do Rio Grande do Sul (FAPERGS) - Brasil. A.S.B. acknowledges financial support from the National Science Centre under projects No. UMO-2017/26/E/ST9/00703 and UMO-2017/25/B/ST9/02218. This research has made use of NASA's Astrophysics Data System. This paper includes data collected by the TESS mission. Funding for the TESS mission is provided by the NASA's Science Mission Directorate.

References

Althaus, L. G. & Córsico, A. H. 2004, A&A, 417, 1115
Althaus, L. G., Córsico, A. H., Isern, J., & García-Berro, E. 2010, A&A Rev., 18, 471
Althaus, L. G., Córsico, A. H., Kepler, S. O., & Miller Bertolami, M. M. 2008, A&A, 478, 175
Althaus, L. G., Panei, J. A., Miller Bertolami, M. M., et al. 2009, ApJ, 704, 1605
Bailer-Jones, C. A. L., Rybizki, J., Fouesneau, M., Demleitner, M., & Andrae, R. 2021, VizieR Online Data Catalog, I/352
Bédard, A., Bergeron, P., & Fontaine, G. 2017, ApJ, 848, 11
Bell, K. J. 2017, PhD thesis, University of Texas
Bell, K. J., Córsico, A. H., Bischoff-Kim, A., et al. 2019, A&A, 632, A42
Bell, K. J., Hermes, J. J., Vanderbosch, Z., et al. 2017, ApJ, 851, 24

Bischoff-Kim, A. & Montgomery, M. H. 2018, AJ, 155, 187
Bischoff-Kim, A. & Østensen, R. H. 2011, ApJ, 742, L16
Bischoff-Kim, A., Østensen, R. H., Hermes, J. J., & Provencal, J. L. 2014, ApJ, 794, 39
Bischoff-Kim, A., Provencal, J. L., Bradley, P. A., et al. 2019, ApJ, 871, 13
Bognár, Z., Paparó, M., Córsico, A. H., Kepler, S. O., & Győrffy, Á. 2014, A&A, 570, A116
Bohm, K. H. & Cassinelli, J. 1971, A&A, 12, 21
Borucki, W. J., Koch, D., Basri, G., et al. 2010, Science, 327, 977
Bradley, P. A. & Winget, D. E. 1994, ApJ, 430, 850
Bradley, P. A., Winget, D. E., & Wood, M. A. 1993, ApJ, 406, 661
Brassard, P., Fontaine, G., Wesemael, F., & Hansen, C. J. 1992, ApJS, 80, 369
Brickhill, A. J. 1991, MNRAS, 251, 673
Charpinet, S., Brassard, P., Giammichele, N., & Fontaine, G. 2019, A&A, 628, L2
Córsico, A. H. 2020, Frontiers in Astronomy and Space Sciences, 7, 47
Córsico, A. H. & Althaus, L. G. 2006, A&A, 454, 863
Córsico, A. H., Althaus, L. G., Benvenuto, O. G., & Serenelli, A. M. 2002, A&A, 387, 531
Córsico, A. H., Althaus, L. G., Kawaler, S. D., et al. 2011, MNRAS, 418, 2519
Córsico, A. H., Althaus, L. G., & Miller Bertolami, M. M. 2006, A&A, 458, 259
Córsico, A. H., Althaus, L. G., Miller Bertolami, M. M., & Bischoff-Kim, A. 2012, A&A, 541, A42
Córsico, A. H., Althaus, L. G., Miller Bertolami, M. M., & García-Berro, E. 2009, in Journal of Physics Conference Series, Vol. 172, Journal of Physics Conference Series, 012075
Córsico, A. H., Althaus, L. G., Miller Bertolami, M. M., & Kepler, S. O. 2019, A&A Rev., 27, 7
Córsico, A. H., Althaus, L. G., Miller Bertolami, M. M., Kepler, S. O., & García-Berro, E. 2014, J. Cosmology Astropart. Phys., 8, 054
Córsico, A. H., Uzundag, M., Kepler, S. O., et al. 2021, A&A, 645, A117
Cox, A. N. 2000, Allen's astrophysical quantities
Dehner, B. T. & Kawaler, S. D. 1995, ApJ, 445, L141
Dupret, M. A., Quirion, P. O., Fontaine, G., Brassard, P., & Grigahcène, A. 2008, in Journal of Physics Conference Series, Vol. 118, Journal of Physics Conference Series, 012051
Fontaine, G. & Brassard, P. 2002, ApJ, 581, L33
—. 2008, PASP, 120, 1043
Giammichele, N., Charpinet, S., Fontaine, G., et al. 2018, Nature, 554, 73
Goldreich, P. & Wu, Y. 1999, ApJ, 511, 904
Hermes, J. J., Gänsicke, B. T., Kawaler, S. D., et al. 2017a, ApJS, 232, 23
Hermes, J. J., Kawaler, S. D., Bischoff-Kim, A., et al. 2017b, ApJ, 835, 277
Howell, S. B., Sobeck, C., Haas, M., et al. 2014, PASP, 126, 398
Kawaler, S. D. 1988, in IAU Symposium, Vol. 123, Advances in Helio- and Asteroseismology, ed. J. Christensen-Dalsgaard & S. Frandsen, 329
Kawaler, S. D. & Bradley, P. A. 1994, ApJ, 427, 415
Kawaler, S. D., Sekii, T., & Gough, D. 1999, ApJ, 516, 349
Kepler, S. O. 1993, Baltic Astronomy, 2, 515
Kepler, S. O., Nather, R. E., Winget, D. E., et al. 2003, A&A, 401, 639
Kepler, S. O., Pelisoli, I., Koester, D., et al. 2015, MNRAS, 446, 4078
—. 2016, MNRAS, 455, 3413
—. 2019a, MNRAS, 486, 2169
—. 2019b, MNRAS, 486, 2169
Kleinman, S. J., Kepler, S. O., Koester, D., et al. 2013, ApJS, 204, 5
Kleinman, S. J., Nather, R. E., Winget, D. E., et al. 1998, ApJ, 495, 424
Koen, C. & Laney, D. 2000, MNRAS, 311, 636
Koester, D., Provencal, J., & Gänsicke, B. T. 2014, A&A, 568, A118
Landolt, A. U. 1968, ApJ, 153, 151
Ledoux, P. & Walraven, T. 1958, Handbuch der Physik, 51, 353
Metcalfe, T. S. 2003, ApJ, 587, L43
Metcalfe, T. S., Nather, R. E., & Winget, D. E. 2000, ApJ, 545, 974
Metcalfe, T. S., Winget, D. E., & Charbonneau, P. 2001, ApJ, 557, 1021
Montgomery, M. H., Hermes, J. J., Winget, D. E., Dunlap, B. H., & Bell, K. J. 2020, ApJ, 890, 11
Nather, R. E., Winget, D. E., Clemens, J. C., Hansen, C. J., & Hine, B. P. 1990, ApJ, 361, 309
Nitta, A., Koester, D., Chu, D., et al. 2012, in Astronomical Society of the Pacific Conference Series, Vol. 462, Progress in Solar/Stellar Physics with Helio- and Asteroseismology, ed. H. Shibahashi, M. Takata, & A. E. Lynas-Gray, 171
O'Donoghue, D. 1994, MNRAS, 270, 222
Østensen, R. H., Bloemen, S., Vučković, M., et al. 2011, ApJ, 736, L39
Provencal, J. L., Montgomery, M. H., Kanaan, A., et al. 2009, ApJ, 693, 564
Quirion, P.-O., Dupret, M.-A., Fontaine, G., Brassard, P., & Grigahcène, A. 2008, in Astronomical Society of the Pacific Conference Series, Vol. 391, Hydrogen-Deficient Stars, ed. A. Werner & T. Rauch, 183
Ricker, G. R., Winn, J. N., Vanderspek, R., et al. 2015, Journal of Astronomical Telescopes, Instruments, and Systems, 1, 014003
Rolland, B., Bergeron, P., & Fontaine, G. 2018, ApJ, 857, 56
Tassoul, M. 1980, ApJs, 43, 469
Tassoul, M., Fontaine, G., & Winget, D. E. 1990, ApJs, 72, 335
Unno, W., Osaki, Y., Ando, H., Saio, H., & Shibahashi, H. 1989, Nonradial oscillations of stars
Uzundag, M., Córsico, A. H., Kepler, S. O., et al. 2021, arXiv e-prints, arXiv:2108.11093
Van Grootel, V., Fontaine, G., Brassard, P., & Dupret, M.-A. 2017, in Astronomical Society of the Pacific Conference Series, Vol. 509, 20th European White Dwarf Workshop, ed. P.-E. Tremblay, B. Gaensicke, & T. Marsh, 321
Voss, B., Koester, D., Napiwotzki, R., Christlieb, N., & Reimers, D. 2007, A&A, 470, 1079
Vuille, F., O'Donoghue, D., Buckley, D. A. H., et al. 2000, MNRAS, 314, 689
Winget, D. E., Hansen, C. J., & van Horn, H. M. 1983a, Nature, 303, 781
Winget, D. E. & Kepler, S. O. 2008, ARA&A, 46, 157
Winget, D. E., Nather, R. E., Clemens, J. C., et al. 1994, ApJ, 430, 839
Winget, D. E., Robinson, E. L., Nather, R. D., & Fontaine, G. 1982a, ApJ, 262, L11
Winget, D. E., van Horn, H. M., Tassoul, M., et al. 1982b, ApJ, 252, L65
Winget, D. E., van Horn, H. M., Tassoul, M., Hansen, C. J., & Fontaine, G. 1983b, ApJ, 268, L33
Wu, Y. & Goldreich, P. 1999, ApJ, 519, 783
York, D. G., Adelman, J., Anderson, Jr., J. E., et al. 2000, AJ, 120, 1579